Contents lists available at ScienceDirect

Applied Catalysis B: Environmental

journal homepage: www.elsevier.com/locate/apcatb

Strong electronic interaction of indium oxide with palladium single atoms induced by quenching toward enhanced hydrogenation of nitrobenzene

Zhijun Li [a],[*], Mingyang Zhang [a], Xiuli Dong [a], Siqi Ji [a], Lili Zhang [b], Leipeng Leng [a], Honghong Li [a], J. Hugh Horton [a],[c], Qian Xu [d], Junfa Zhu [d]

[a] *Joint International Research Laboratory of Advanced Chemical Catalytic Materials & Surface Science, College of Chemistry and Chemical Engineering, Northeast Petroleum University, Daqing 163318, PR China*
[b] *Shenyang National Laboratory for Materials Science, Institute of Metal Research, Chinese Academy of Sciences, Shenyang 110016, PR China*
[c] *Department of Chemistry, Queen's University, 90 Bader Lane, Kingston K7L 3N6, Ontario, Canada*
[d] *National Synchrotron Radiation Laboratory, University of Science and Technology of China, Hefei 230029, PR China*

ARTICLE INFO

ABSTRACT

The realization of efficient and fully controllable synthesis of single atom catalysts is an exciting frontier, yet still challenging in the modern catalysis field. Here we describe a straightforward high-temperature quenching approach to precisely construct isolated palladium atoms supported over cubic indium oxide, with individual palladium atoms coordinated with four neighboring oxygen atoms. This palladium catalyst achieves exceptional catalytic efficiency in the selective hydrogenation of nitrobenzene to aniline, with more than 99% chemo-selectivity under almost 100% conversion. Moreover, it delivers excellent recyclability, anti-CO poisoning ability, storage stability, and substrate tolerance. DFT calculations further reveal that the high catalytic activity stems from the optimized electronic structure and the charge states of palladium atoms in the defect-containing indium oxide. Our findings provide an effective approach to engineering single atom catalysts at the atomic level and open the door to a wide variety of catalytic reactions.

1. Introduction

Anilines and their derivatives are important chemicals and key intermediates for the synthesis of pharmaceuticals, dyes, agrochemicals, and other value-added chemical reagents [1,2]. Selective hydrogenation of nitroarenes with supported metal catalysts is recognized as an efficient and environmentally benign treatment to produce anilines [3,4]. However, the harsh operating conditions (high temperatures and pressures) and inevitable by-products such as nitroso- and azo-compounds have greatly hampered the catalysts' efficiency [3,5]. Therefore, the creation of efficient and environmentally friendly catalyst systems, ideally working under mild conditions, for selective hydrogenation of nitroarenes is significantly important for fundamental studies and industrial applications.

Recently, single atom catalysts (SACs) have received extensive attention and have been recognized as a frontier of heterogeneous catalysis because of their efficient metal utilization and unique catalytic activity [6–12]. The maximized atom exposure, with the accessibility of the active sites to the reactants, is a key factor for the unique geometric and electronic structures that ultimately contribute to the overall performance of the catalysts [8,13–17]. But such isolated metal atoms with large surface free energy have a high propensity to aggregate under harsh reaction conditions, leading to degradation of catalytic activity [18–21]. This challenge can be solved by increasing the metal-support interactions by the optimum coordination of the neighboring heteroatoms [22–24]. In this context, various engineering strategies have been applied to develop better SACs, such as atomic layer deposition (ALD), thermal emitting, mass-selected soft landing, etc. [6,25–27]. Although these methods can control the surface composition and morphology of catalysts at the atomic scale, many involve complex synthesis processes, sophisticated/expensive equipments, or laborious post-modifications. These problems are obstacles to the large-scale production of SACs. Therefore, an efficient, low-cost, and general strategy for the synthesis of SACs is highly desired.

Indium oxide (In_2O_3), with a bixbyite structure, is a reducible oxide with n-type conductivity [28,29]. It has been validated as a promising catalyst with a rich electronic structure for the synthesis of methanol and semihydrogenation reactions [30–32]. Pérez-Ramírez et al. studied the

outstanding semihydrogenation performance of In_2O_3 and concluded that the O atom vacancies resulted in In_3O_5 moieties serve as the catalytic active sites [33]. Huang et al. describe a single Ir atom catalyst (Ir_1/In_2O_3) in which the Ir coordinates with the adjacent oxygen vacancy to form a Lewis acid-base pair, showing high efficiency for hydrogenation of CO_2 to ethanol [34]. Pérez-Ramírez et al. report a co-precipitation approach to access single palladium atoms in the In_2O_3 lattice forming low-nuclearity palladium clusters to produce methanol via CO_2 hydrogenation [35]. Liu and co-workers employed density functional theory (DFT) calculations to study the favorable role of Pt_4/In_2O_3 and the underlying mechanism of methanol synthesis from CO_2 hydrogenation [36].

In this work, we report a straightforward high-temperature quenching approach to efficiently access atomically dispersed palladium atoms deposited over cubic indium oxide (Pd_1/In_2O_{3-x}). A range of materials characterization methods and density functional theory (DFT) calculations confirm the presence of single palladium atoms over defective In_2O_3, with each palladium atom coordinated with four neighboring oxygen atoms. The Pd_1/In_2O_{3-x} catalyst delivered superior catalytic efficiency in the selective hydrogenation of nitrobenzene to aniline, along with excellent recyclability, storage stability, and substrate tolerance. Moreover, it demonstrated exceptional anti-CO poisoning ability during the hydrogenation reaction in CO-contaminated hydrogen. DFT calculations further reveal that the high catalytic activity originates from the unique electronic structure of palladium sites in the defect-containing indium oxide.

2. Experimental sections

2.1. Chemicals

All chemical reagents were used without further purification. Indium nitrate hydrate, sodium hydroxide, sodium tetrachloropalladate(II), palladium(II) chloride, nitrobenzene, urea, 1-chloro-4-nitrobenzene, 1-chloro-3-nitrobenzene, 1-chloro-2-nitrobenzene, 1-bromo-4-nitrobenzene, 1-fluoro-4-nitrobenzene, 1-fluoro-2-nitrobenzene, 4-nitrobenzaldehyde, 4-nitroanisole, 4-nitrobenzoic acid, 2-nitrobenzoic acid, 4-nitrotoluene, 3-nitrotoluene, 4-nitrobenzyl alcohol, 4-nitroaniline, 1,3-dinitrobenzene, 4-nitrophenol, ethanol, methanol, 1-butanol, isopropyl alcohol, dodecane, toluene, zinc nitrate hexahydrate, and 2-methylimidazole were purchased from Aladdin. Commercial carbon-supported Pd (5 wt%) was supplied by Aldrich.

2.2. Synthesis of the catalysts

Synthesis of cubic In_2O_3: In a typical synthesis, 0.7 g of $In(NO_3)_3 \cdot xH_2O$ and 0.6 g of NaOH were dissolved in 70 mL of methanol to form solutions A and B, respectively. Then, solution A was introduced into solution B under sonication for 1 h. After that, the mixture was transferred into a 200 mL of Teflon-lined autoclave and heated at 250 °C for 24 h. The precipitate was washed with distilled water and dried in vacuum at 80 °C for 12 h. Then, the resulting white powder was thermally treated at 500 °C for 3 h in air to give yellow-colored cubic In_2O_3.

Synthesis of Pd_1/In_2O_{3-x}: In a typical synthesis, 100 mg of as-prepared In_2O_3 with a high temperature of 500 °C was immediately removed from the tube furnace and introduced into an aqueous solution (50 mL) containing 80 µL of Na_2PdCl_4 solution (10 mg mL^{-1}) at 0 °C by an ice water mixture for 10 min with stirring. The product was washed and vacuum dried at 80 °C for 12 h. The resulting sample is designated as Pd_1/In_2O_{3-x}. The Pd loading of the sample was measured to be 0.34 wt% based on ICP-AES test. **Safety Note**: Owing to the high temperature, special cautions should be paid.

Synthesis of Pd_1/In_2O_{3-x}-L: The synthetic method is similar to that of Pd_1/In_2O_{3-x}, except 40 µL of Na_2PdCl_4 aqueous solution (10 mg mL^{-1}) was used. The Pd loading of the sample was measured to be 0.18 wt% based on ICP-AES test.

Synthesis of Pd_1/In_2O_{3-x}-H: The synthetic method is similar to that of Pd_1/In_2O_{3-x}, except 100 µL of Na_2PdCl_4 aqueous solution (10 mg mL^{-1}) was used. The Pd loading of the sample was measured to be 0.47 wt% based on ICP-AES test.

Synthesis of Pd NPs/In_2O_{3-x}: The synthetic method is similar to that of Pd_1/In_2O_{3-x}, except 40 µL of Na_2PdCl_4 aqueous solution (100 mg mL^{-1}) was used. The Pd loading of the sample was measured to be 2.42 wt% based on ICP-AES test.

Synthesis of In_2O_{3-x}: The synthetic method is similar to that of Pd_1/In_2O_{3-x}, except no palladium salt solution was used.

Synthesis of Pd_1/C_3N_4: The synthetic method is based on a previously reported work [37].

Synthesis of Pd_1/In_2O_3-I: In a typical synthesis, 100 mg of In_2O_3 was added to an aqueous solution (50 mL) containing 40 µL of Na_2PdCl_4 solution (10 mg mL^{-1}) with vigorous stirring at 80 °C in an oil bath until the water was evaporated. The resulting powder was transferred to an alumina crucible and underwent a thermal treatment in an ambient environment oven with a heating rate of 2 °C/min from room temperature to 350 °C for 2 h. The Pd loading in the catalyst was 0.21 wt% based on ICP-AES test.

3. Results and discussions

3.1. Synthesis and characterizations of the isolated Pd catalysts

Here we developed an effective quenching strategy to access single palladium atoms over indium oxide with each palladium atom coordinated with four neighboring oxygen atoms (Pd_1/In_2O_{3-x}). In a typical synthesis (Fig. 1a), cubic In_2O_3 was synthesized by a solvothermal treatment followed by calcination in air (Fig. S1). The resulting In_2O_3 at 500 °C was immediately introduced into an aqueous palladium salt solution at 0 °C, cooled by ice-cold deionized water, for rapid quenching. The as-prepared catalyst was denoted as Pd_1/In_2O_{3-x} and the corresponding Pd loading was 0.34 wt%.

A lower Pd loading reference (0.18 wt%) was created by using a low dose of Pd salt (denoted as Pd_1/In_2O_{3-x}-L), as shown in Fig. S2. Another reference sample, denoted as In_2O_{3-x}, was prepared in the absence of Pd salt (Fig. S3). A 2.42 wt% Pd nanoparticle-containing catalyst (Pd NPs/In_2O_{3-x}) was also prepared using a high concentration palladium salt solution (Fig. S4). Unlike the yellow-colored In_2O_3, the In_2O_{3-x}, Pd_1/In_2O_{3-x}, and Pd NPs/In_2O_{3-x} displayed different colors (Fig. S5). In Fig. 1b–d, scanning electron microscope (SEM), high-angle annular dark-field scanning transmission electron microscope (HAADF-STEM), and transmission electron microscope (TEM) images show that the cubic structure was retained for Pd_1/In_2O_{3-x} after the quenching treatment, but with slightly morphology change. A high-resolution transmission electron microscope (HR-TEM) image (Fig. 1d inset) displays a lattice spacing of 0.292 nm corresponding to the (222) plane of In_2O_{3-x}. Aberration-corrected HAADF-STEM imaging reveals the isolated palladium atoms, which have a lower Z contrast than indium atoms, are homogeneously distributed over the support (Fig. 1e and S6). We note that the smooth surface of cubic In_2O_3 transformed into a jagged (step-like) surface that rich in defects. This might be due to the combined effects of quenching and palladium atom doping. The intensity profile further shows the evidence of atomically dispersed palladium atoms. A determination of palladium dispersion in samples was attempted by CO titration. The palladium dispersion in Pd_1/In_2O_{3-x} was calculated to be nearly 98% (Table S1) and this indicates the palladium atoms over the support predominantly feature as highly dispersed single atoms [38,39]. The elemental mapping shows the uniform distribution of O, In, and Pd atoms (Fig. 1f).

The crystalline structure of the samples was evaluated by X-ray diffraction (XRD) analysis (Fig. 2a). All samples showed similar characteristic diffraction peaks that can be assigned to the cubic In_2O_3 (JCPD 06--0416). No diffraction peaks of metallic palladium species were detected for Pd_1/In_2O_{3-x}, indicating the high dispersion or low content

a

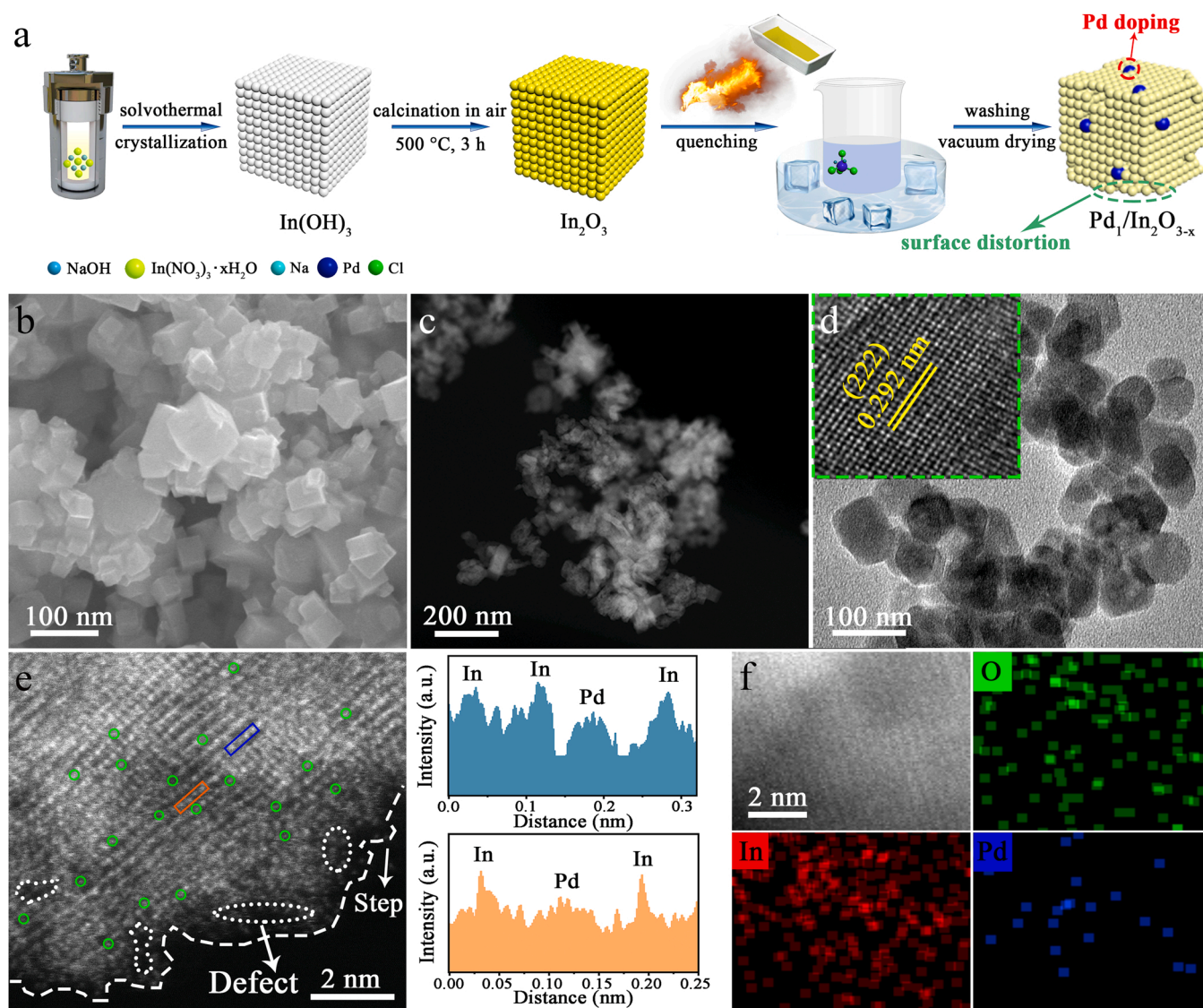**Fig. 1.** Synthesis and structural characterization of Pd_1/In_2O_{3-x}. (a) Schematic illustration for the construction of Pd_1/In_2O_{3-x}. (b) SEM, (c) HAADF-STEM, (d) TEM and HR-TEM images. (e) AC HAADF-STEM image and intensity profile analysis. (f) STEM-EDS elemental mapping.

of palladium atoms over the support [40]. By contrast, typical metallic palladium peaks were noticed on Pd NPs/In_2O_{3-x}. Raman spectra of samples are shown in Fig. 2b. A high-intensity peak at 132 cm^{-1} was associated with the In−O vibration of an octahedral InO_6 structure [41]. The peaks at 305 and 495 cm^{-1} were ascribed to the bending and stretching vibration of the octahedral InO_6 in In_2O_3 [42]. Moreover, the peak at 364 cm^{-1} corresponds to the stretching vibration of In−O−In, which implies the existence of oxygen vacancies [43]. The ratio of the peaks at 364 (I_2) and 305 cm^{-1} (I_1) is typically used to show the number of oxygen vacancies [44]. The I_2/I_1 ratios for In_2O_3 and In_2O_{3-x} were calculated to be 0.08 and 0.22, respectively. It suggests more oxygen vacancies were generated in In_2O_3 by the quenching treatment. After doping with palladium species, the I_2/I_1 ratios were observed to be 0.24, 0.25, and 0.16 for Pd_1/In_2O_{3-x}-L, Pd_1/In_2O_{3-x}, and Pd NPs/In_2O_{3-x}, respectively. This suggests that a low amount of Pd doping facilitates the generation of oxygen vacancies while a higher amount of Pd atoms doping tends to block a portion of oxygen vacancies.

X-ray photoelectron spectroscopy (XPS) results show the presence of C, O, In, and Pd elements in Pd_1/In_2O_{3-x} (Fig. S7). For In 3d spectrum (Fig. S8a), two peaks at 444.2 and 451.7 eV are associated with the spin-orbit of In3d$_{5/2}$ and In 3d$_{7/2}$, respectively [44]. No obvious peak shift was observed in the In 3d spectrum for In_2O_{3-x} and Pd_1/In_2O_{3-x}. This

suggests that the chemical environment of In might not be greatly affected by the Pd doping. The O 1s spectrum (Fig. S8b) can be deconvoluted into three peaks that are associated with lattice oxygen at 529.8 eV, oxygen defect sites at 530.9 eV, and surface adsorbed hydroxyl species at 532.1 eV, respectively [45]. We observe that the oxygen vacancy ratio was increased after Pd doping from 17.8% to 29.4%, in line with the Raman results. In the case of the Pd 3d spectrum (Fig. 2c), the Pd$_{5/2}$ peak of Pd_1/In_2O_{3-x} was centered at 336.7 eV, implying the palladium species in the catalyst have a higher oxidation state [13,44,46]. The X-ray absorption near-edge structure (XANES) and extended X-ray absorption fine structure (EXAFS) were collected to determine the dispersion of palladium atoms in Pd_1/In_2O_{3-x}. The XANES spectra display the energy absorption threshold of Pd_1/In_2O_{3-x} is intermediate to those of Pd foil and PdO, indicating the valence of the Pd atom in the catalyst is between Pd^0 and Pd^{2+} (Fig. 2d). The k^3-weighted Fourier transform EXAFS data (without phase correction) are shown in Fig. 2e. A Pd foil exhibits a notable peak at 2.48 Å that is associated with the Pd–Pd coordination. In the case of PdO, two main peaks at 1.57 Å and 2.99 Å correspond to Pd−O and Pd−O−Pd in the first and second coordination shells, respectively. The Pd_1/In_2O_{3-x} shows one dominant peak at 1.57 Å that can be assigned to Pd−O coordination. In addition, no obvious Pd−Pd coordination can be found,
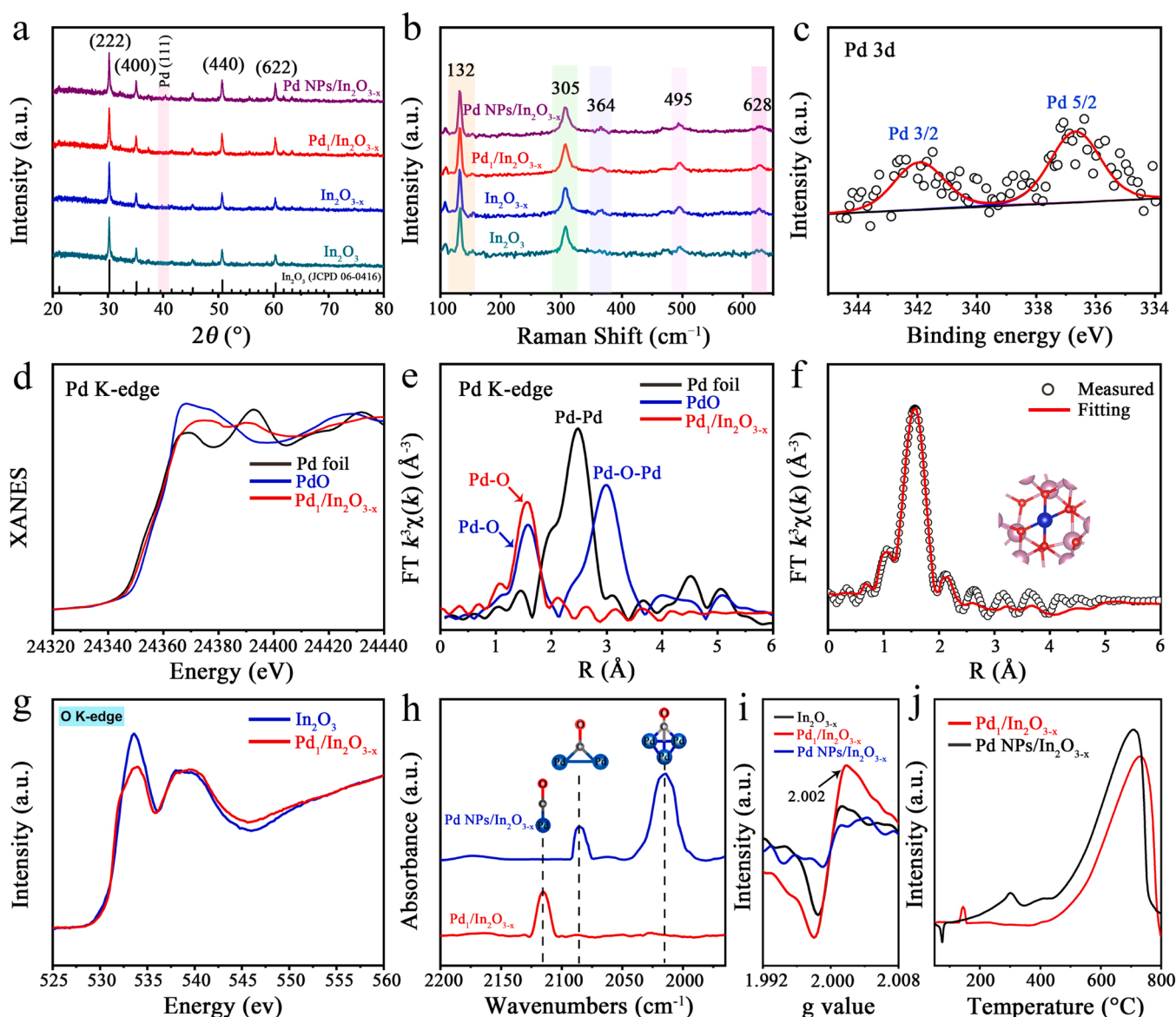
Fig. 2. Characterization of Pd_1/In_2O_{3-x}. (a) XRD patterns. (b) Raman spectra. (c) High-resolution XPS Pd 3d spectrum. (d) Pd K-edge XANES spectra. (e) FT k^3-weighted Pd K-edge EXAFS spectra. (f) EXAFS fitting results. (g) O K-edge spectra. (h) CO-DRIFTS spectra. (i) EPR results. (j) H_2-TPR results.

suggesting the atomic dispersion of palladium atoms over the support. EXAFS fitting was conducted and the palladium atom exhibits a coordination number of four, directly connected to four oxygen atoms with a mean bond length of 2.02 Å (Fig. 2f and Table S2). The O K-edge spectra of In_2O_3 and Pd_1/In_2O_{3-x} were shown in Fig. 2g. The decreased peak intensity at 533.7 eV of Pd_1/In_2O_{3-x} can be ascribed to defect generation and Pd doping [34]. Diffuse reflectance infrared Fourier transform spectroscopy (DRIFTS) of CO adsorbed on the catalysts was measured to distinguish the isolated palladium atoms in the catalyst (Fig. 2h). For Pd_1/In_2O_{3-x}, the absorption peak centered at 2116 cm^{-1} was assigned to the linear-adsorbed CO on cationic Pd single atoms in an on-top configuration [47]. In the case of Pd NPs/In_2O_{3-x}, two peaks at 2086 and 2014 cm^{-1} were observed that correspond to the bridge-adsorbed and threefold-hollow-adsorbed CO on Pd clusters, respectively [48]. Electron paramagnetic resonance (EPR) spectra of samples were collected and a sharp signal at a g value of 2.002 was observed for Pd_1/In_2O_{3-x} (Fig. 2i). Together, the combination results of AC HAADF STEM, CO titration, XPS, EXAFS, CO DRIFTS, and EPR strongly support the existence of single palladium atoms in the catalyst.

Fourier transform infrared spectroscopy (FT-IR) analysis shows typical features of In_2O_3 in these samples (Fig. S9). Absorption peaks at $420 \sim 612\ cm^{-1}$ are assigned to the stretching and bending vibrations of In_2O_3 [49]. H_2-TPR profiles of samples are shown in Fig. 2j. For Pd_1/In_2O_{3-x}, a peak at 143 °C corresponds to the reduction of Pd species in Pd_1/In_2O_{3-x}, which implies a stronger interaction between isolated palladium atoms and support [13,50]. For Pd NPs/ In_2O_{3-x}, a negative peak at 71 °C originates from the decomposition of palladium hydride [51]. The peak at 301 °C corresponds to the reduction of In_2O_3 surface and the generation of oxygen vacancies [29]. For higher reduction temperatures (> 700 °C), we observe the supported Pd NPs could help to decrease the reduction temperature and further reduction of indium species [51]. The specific surface areas of samples were measured by N_2 adsorption/desorption isotherms (Fig. S10). The corresponding results for In_2O_3, Pd_1/In_2O_{3-x}, and Pd NPs/In_2O_{3-x} were measured to be 18.92, 19.17, and 18.44 m^2/g, respectively.

Density functional theory (DFT) calculations were performed to unravel the most likely structure of Pd atoms over In_2O_3. Based on a previously reported work by Pérez-Ramírez et al. [35], the palladium atom was found to have a high propensity to replace the indium atom in In_2O_3 lattice, and the palladium atom was more stable at a surface site

rather than in a bulk site. Here, a defect-containing In_2O_3 (111) surface was created by removal of an oxygen atom. Three Pd sites at different positions over defective In_2O_3 were constructed for screening (Fig. S11a). After relaxation, the most stable Pd site was found to be position 2, a square planar coordination with an average Pd-O bond length of 2.06 Å, with the lowest formation energy of 2.96 eV (Fig. S11b). This is in good agreement with the XAFS results. The charge density distribution of the three Pd doping sites displayed the detailed bonding information in Fig. S12-S14. The coordination structures between Pd and O for positions 1–3 are Pd1-O3, Pd1-O4, and Pd1-O4, respectively. The projected density of states (pDOS) of Pd in three different locations showed that the intensity of Pd state in Position 2 has the highest intensity (Fig. S11c), implying that there are more empty d orbitals near the Fermi level which would greatly favor reactant adsorption and activation. These findings suggest that the introduction of Pd atoms into the defective In_2O_3 support can significantly modify the electronic properties of the catalyst because of the electronic metal-support interaction.

3.2. Catalytic performance of the isolated Pd catalysts

The catalytic performance of Pd_1/In_2O_{3-x} towards hydrogenation of nitrobenzene was examined under mild conditions of 1 atm H_2 at 20 °C (Fig. 3). Nitrobenzene was selected as a model substrate. Home-made Pd single atoms supported over carbon nitride (Pd_1/C_3N_4), Pd single atoms stabilized over nitrogen-doped carbon (Pd_1/N-C), and commercial Pd/C (5 wt%) and H_2PdCl_4 were used as reference samples (Fig. S15-S17). Additionally, Pd single atoms distributed over In_2O_3 by an impregnation method was fabricated (Pd_1/In_2O_3-I), as shown in Fig. S18. We initially screened the different solvents and found that water was the optimum solvent in our catalytic system (Fig. 3a and Table S3). No reaction was observed with either In_2O_3 or In_2O_{3-x} (Table S4). In sharp contrast, the use of Pd_1/In_2O_{3-x} showed an exceptionally high catalytic activity with a turnover frequency (TOF) of 4286 h^{-1}, along with a conversion of 99% and a selectivity of 99% towards aniline within 30 min (Fig. 3b,c and Fig. S19). Moreover, the conversion and selectivity remain consistent when prolonging the reaction time to 12 h (Fig. S20), demonstrating the high selectivity of Pd_1/In_2O_{3-x}. Hot filtration (Fig. S21) and ICP-AES tests confirmed no palladium leaching during the reaction. $Pd_1/$
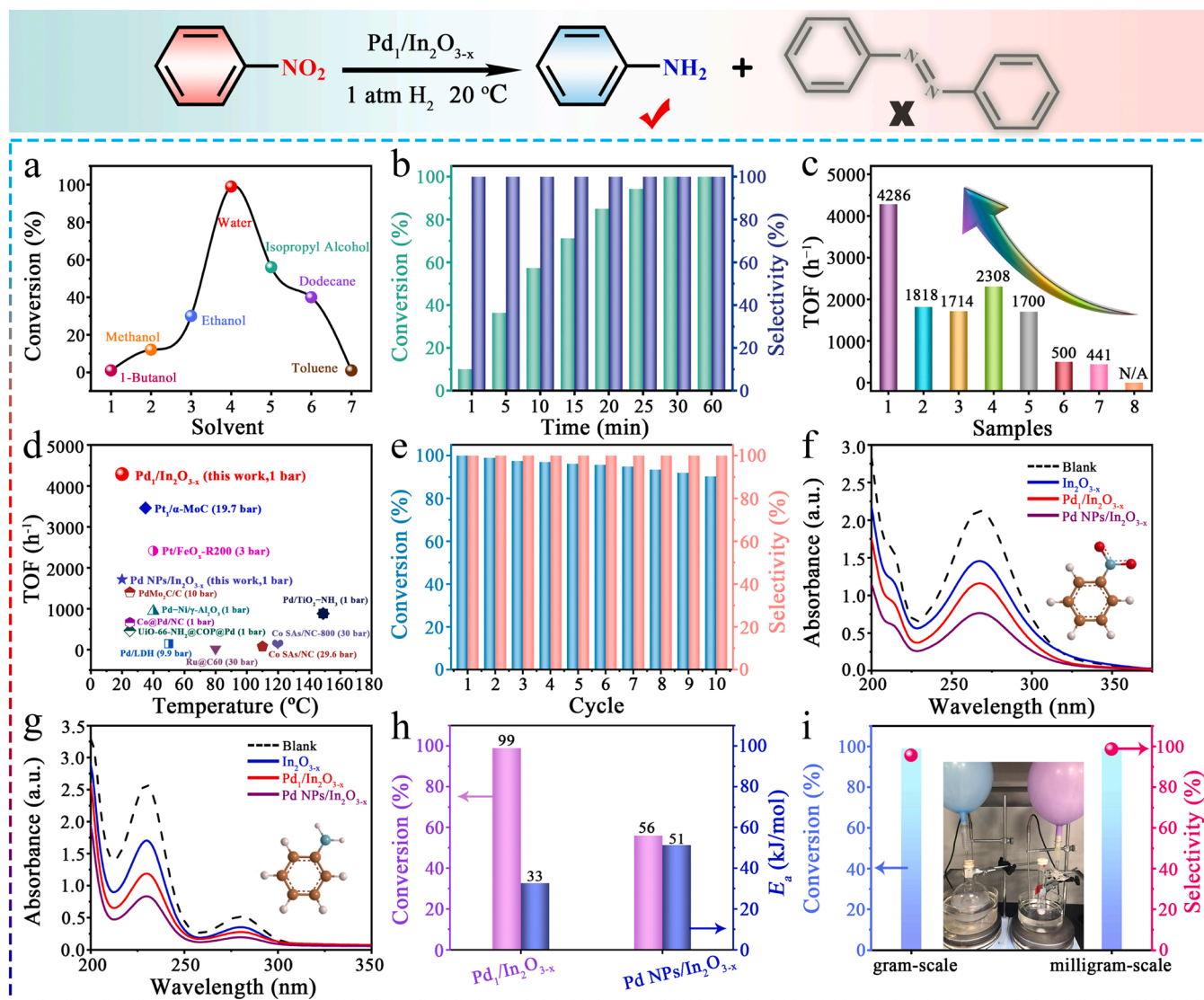

Fig. 3. Catalytic performance of Pd_1/In_2O_{3-x} in the hydrogenation of nitrobenzene. (a) Solvent selection. (b) Conversion and selectivity. (c) TOF values. (d) Comparison of TOF values with reported catalyst systems. (e) Recycling results. UV–vis diffuse reflectance absorption spectra of (f) nitrobenzene and (g) aniline on samples. (h) Comparison in conversion and E_a. (i) Scale up reactions. (Samples: 1: Pd_1/In_2O_{3-x}, 2: Pd_1/In_2O_{3-x}-L, 3: Pd NPs/In_2O_{3-x}, 4: 5% Pd/C, 5: H_2PdCl_4, 6: Pd_1/In_2O_3-I, 7: Pd_1/N-C, 8: Pd_1/C_3N_4).

In$_2$O$_{3-x}$-L exhibited a low TOF of 1818 h^{-1} which might result from the limited number of active Pd sites. The use of Pd NPs/In$_2$O$_{3-x}$ and Pd/C yielded aniline with low TOF values of 1714 and 2308 h^{-1}, respectively, along with a slow nitrobenzene conversion. A higher Pd loading catalyst (Pd$_1$/In$_2$O$_{3-x}$-H, Pd loading of 0.47 wt%) was prepared (Fig. S22a-c) by the quenching approach and the corresponding defects (I$_2$/I$_1$ = 0.21) were less when compared with that of 0.25 for Pd$_1$/In$_2$O$_{3-x}$. This is consistent with our findings that a low amount of Pd doping facilitates the generation of oxygen vacancies while a higher amount of Pd atoms doping tends to block a certain amount of oxygen vacancies. The catalytic activity of Pd$_1$/In$_2$O$_{3-x}$-H was found to be inferior to that of Pd$_1$/In$_2$O$_{3-x}$ but higher than Pd NPs/In$_2$O$_{3-x}$ (Fig. S22d). With the use of H$_2$PdCl$_4$, a TOF value of 1700 h^{-1} was obtained. Pd$_1$/In$_2$O$_3$-I, Pd$_1$/N-C, and Pd$_1$/C$_3$N$_4$ showed extremely poor catalytic activity and gave trace products. These control samples highlight the effectiveness of Pd$_1$/In$_2$O$_{3-x}$ in catalyzing this reaction. Impressively, Pd$_1$/In$_2$O$_{3-x}$ showed extremely high catalytic activity, especially at lower reaction temperature and pressure, outperforming those of previously reported studies (Fig. 3d and Table S5). Notably, it delivered excellent recycling stability (successive 10 rounds) in both conversion and selectivity (Fig. 3e). Characterization of the spent catalyst after recycling showed no obvious structural change (Fig. S23) and no palladium leaching in the reaction solvent by ICP-AES. This results from the strong electronic metal–support interaction between Pd and In$_2$O$_{3-x}$ support. The AC-STEM image (Fig. S23c) and CO adsorbed IR spectrum (Fig. S23f) excluded the presence of Pd agglomeration over the support. Moreover, EXAFS results further evidenced the absence of Pd—Pd bond and the presence of Pd1–O4 moieties in the spent catalyst (Fig. S24 and Table S2). These results strongly demonstrate the robust nature of Pd$_1$/In$_2$O$_{3-x}$ catalyst.

Adsorption experimental results (Fig. 3f) show that Pd NPs/In$_2$O$_{3-x}$ has the highest adsorption tendency for nitrobenzene. This was followed by Pd$_1$/In$_2$O$_{3-x}$ and In$_2$O$_{3-x}$. In addition, we observe the adsorption ability of Pd$_1$/In$_2$O$_{3-x}$ for aniline is less than that of Pd NPs/In$_2$O$_{3-x}$ (Fig. 3 g). Based on this evidence, the adsorption behavior of Pd$_1$/In$_2$O$_{3-x}$ was found to favor the selective hydrogenation of nitrobenzene to aniline. Kinetic studies were further conducted over Pd$_1$/In$_2$O$_{3-x}$ and Pd NPs/In$_2$O$_{3-x}$ in the temperature ranges of 10–40 °C (Fig. 3h and S25). Pd$_1$/In$_2$O$_{3-x}$ exhibited a low E_a of 33 kJ mol^{-1} with a high conversion efficiency of 99%. The Pd NPs/In$_2$O$_{3-x}$ demonstrated a higher E_a of 51 kJ mol^{-1} but with a lower conversion of 56%. The experimental results presented above indicate that Pd$_1$/In$_2$O$_{3-x}$ can greatly lower the energy barrier to facilitate the initiation of the catalytic reaction. The anti-CO poisoning ability of Pd-based catalysts in CO-contaminated hydrogen was further evaluated (Table S6). The poisoning is associated with the strong adsorption of CO on Pd atoms which might block the active sites from hydrogen adsorption and activation. For Pd$_1$/In$_2$O$_{3-x}$ and Pd$_1$/In$_2$O$_{3-x}$-L, they remained active with excellent conversion and selectivity both in 0.1% and 0.5% CO conditions. In contrast, The Pd NPs/In$_2$O$_{3-x}$ suffered severely from CO poisoning with limited catalytic hydrogenation activity. The commercial Pt/C catalyst was completely poisoned, and no activity was observed even at high temperatures. These results revealed excellent CO-resistant hydrogenation ability of Pd$_1$/In$_2$O$_{3-x}$. Scaling the catalytic reaction up (60-fold) resulted in a comparable efficiency for the target product of aniline (Fig. 3i), highlighting the potential scale tolerance of this catalyst system. Another intriguing feature of the synthetic approach is the promise of scalability in production (up to gram-scale). Due to the relatively facile operations (thermal treatment, quenching, washing, and drying), it readily translates the gram-scale production of the catalyst with no observable differences in the structure and catalytic performance (Fig. S26). After one year of storage in air, the typical atomical features of this catalyst were maintained with satisfactory catalytic activity (Fig. S27).

3.3. Insight into the catalytic behavior

These experiments were further complemented by DFT calculations. The density of states (DOS) was investigated and obvious differences are noticed (Fig. S28-S30). There are many overlapping states between Pd and O below the Fermi level in position 2, suggesting the strong hybridization (bonds forming) between palladium and oxygen orbitals with high charge transfer ability. This also implies a strong electronic metal-support interaction. In addition, In$_2$O$_3$ exhibits semiconductor behavior while Pd$_1$/In$_2$O$_{3-x}$ has states on the Fermi level, indicating a better electronic conductivity. Charge density difference plots demonstrate that Pd atoms on defect-containing In$_2$O$_3$ cause significant charge transfer from the Pd atom to the surrounding O atoms (Fig. 4a and S31). The Pd NPs/In$_2$O$_{3-x}$ was modeled as the optimized Pd$_4$ cluster over the defective In$_2$O$_3$ (111) surface. A similar trend of charge transfer was found for Pd NPs/In$_2$O$_{3-x}$ (Fig. S32). The Bader charge was then calculated to qualitatively compare charge transfer in three different locations and the results are shown in Fig. 4b and S33. The Pd atom in position 2 donates 0.88e, more than those of 0.69e and 0.79e in positions 1 and 2, to the O atoms and forms Pd—O bonds. This suggests a more positive oxidation state of Pd in position 2.

The electronic localization function (ELF) is a position-dependent function and was employed to study the electronic structure of the catalysts (Fig. 4c and S34). In ELFs, 0 denotes the high delocalization electron distribution, and 1 means the high localization electron distribution [36]. The ELF of 0.5 indicates the electron-gas-like pair probability [52]. We observe the electrons transferred from the Pd atom to the nearby oxygen atoms, resulting in a much more electron-gas-like distribution around the oxygen atoms. This is in good agreement with the Bader charge analysis. Partial density of states (pDOS) of Pd$_1$/In$_2$O$_{3-x}$ and Pd NPs/In$_2$O$_{3-x}$ were calculated and the results are shown in Fig. 4d. The d-band center for Pd$_1$/In$_2$O$_{3-x}$ and Pd NPs/In$_2$O$_{3-x}$ was located at − 3.61 and − 0.99 eV, respectively. This suggests that Pd NPs/In$_2$O$_{3-x}$ adsorb nitrobenzene more strongly which may be an obstacle for the catalytic reaction. In addition, a significant overlap between the Pd 3d orbital of Pd$_1$/In$_2$O$_{3-x}$ and O 2p orbital of adsorbed nitrobenzene near the Fermi energy level suggests that the Pd atom in Pd$_1$/In$_2$O$_{3-x}$ serves as the active site for nitrobenzene activation.

The catalytic mechanism in the hydrogenation of nitrobenzene to aniline over Pd$_1$/In$_2$O$_{3-x}$ and Pd NPs/In$_2$O$_{3-x}$ was investigated (Fig. 4e). Here, the indirect hydrogen-induced dissociation pathway was taken into consideration. The PhNO$_2$ molecules are initially adsorbed onto the catalysts' surfaces, with adsorption energies of − 0.97 eV and − 1.89 eV for Pd$_1$/In$_2$O$_{3-x}$ and Pd NPs/In$_2$O$_{3-x}$, respectively. Then, the O terminal of N-O bond was hydrogenated for the activation of N—O bond to yield PhNOOH*. In the case of Pd$_1$/In$_2$O$_{3-x}$ (Table S7), the N—O bond length was 1.25 Å after the PhNO$_2$ adsorption. One oxygen of the nitro group in nitrobenzene was hydrogenated to climb over an energy barrier of 0.87 eV (TS1) with endothermic by merely 0.12 eV. The N—O bond length was elongated from 1.25 to 1.44 Å and this step facilitates the subsequent N—O dissociation. The other oxygen of the nitro group was further hydrogenated with a substantially lower hydrogenation barrier of 0.17 eV (TS2) to give an active PhN(OH)$_2$* intermediate. This step turned to release the energy of 0.18 eV and the corresponding bond lengths of N—O and H—O were 1.41 and 1.43 Å, respectively. Subsequently, one of the N—OH bonds of PhN(OH)$_2$* was dissociated by overcoming an energy barrier of 0.72 eV (TS3) to generate PhNOH* and OH*, along with an N—O bond length of 1.73 Å. This step is exothermic by 0.21 eV and the as-generated OH* can be reduced to water and desorbed from the catalyst's surface. Here, the overall energy barrier of the H-induced dissociation path, from PhNO$_2$* to TS3, was calculated to be 0.66 eV. In the following step, an energy barrier of 0.43 eV (TS4) was required to further hydrogenate the PhNOH* to PhNHOH* and the reaction was exothermic by 0.44 eV. The N—H bond length was 1.57 Å. Then, the N − OH bond was dissociated to give PhNH* and OH* with the highest energy barrier of 0.99 eV (TS5), implying this is the rate-
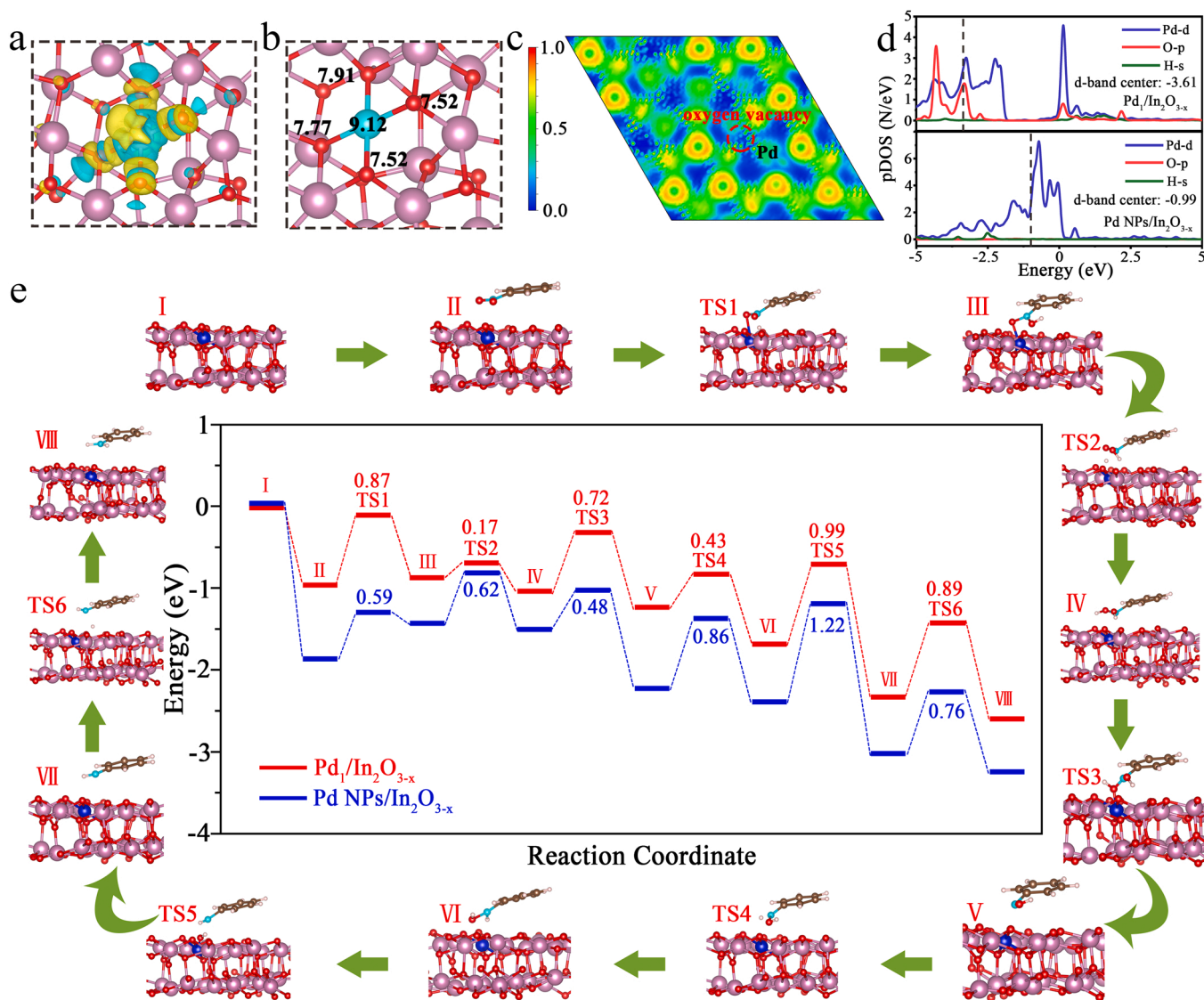
Fig. 4. (a) Charge density difference, (b) Bader charge, and (c) Electronic localization function (ELF) contour of Pd_1/In_2O_{3-x}. (d) Partial density of states (pDOS) of Pd_1/In_2O_{3-x} and Pd NPs/In_2O_{3-x} during nitrobenzene adsorption. (e) Energy profiles of the hydrogenation of nitrobenzene to aniline over Pd_1/In_2O_{3-x} and Pd NPs/In_2O_{3-x}.

determining step. Moreover, this step was highly exothermic by 0.65 eV. After the final step of hydrogenation of PhNH*, the aniline was achieved by conquering an energy barrier of 0.89 eV (TS6) and exothermic by 0.25 eV, along with an N—H bond length of 1.60 Å.

For Pd NPs/In_2O_{3-x} (Fig. S35 and Table S8), the formation of PhN $(OH)_2$* required an activation energy as high as 0.62 eV, which is 0.45 eV higher than that of Pd_1/In_2O_{3-x}. Notably, the first two steps (TS1 to TS2) are highly endothermic by 0.36 eV for Pd NPs/In_2O_{3-x}. However, 0.06 eV energy was released for Pd_1/In_2O_{3-x}. The overall energy barrier of the H-induced dissociation path for Pd NPs/In_2O_{3-x} was 0.18 eV higher than that of Pd_1/In_2O_{3-x}. Because of the high energy barrier for Pd NPs/In_2O_{3-x}, this endothermic reaction is difficult to proceed with. Similarly, the rate-determining step is the transformation of PhNHOH* to PhNH* in TS5 with the highest energy barrier of 1.22 eV, which is 0.23 eV higher than that of Pd_1/In_2O_{3-x}. Particularly, the Pd_1/In_2O_{3-x} was exothermic by 1.61 eV during the whole reaction path, releasing more energy (0.23 eV) than that of Pd NPs/In_2O_{3-x}. Together, the substantially lowered energy barrier and sharp difference in each elementary step between two catalysts demonstrate the catalytic reaction is kinetically and thermodynamically favorable on Pd_1/In_2O_{3-x}.

3.4. Substrate scope of the isolated Pd catalysts

With the high efficiency of Pd_1/In_2O_{3-x} in hand, we next sought out to explore the substrate scope and functional group tolerance with a library of 16 nitrobenzene derivatives (Fig. 5). Excitingly, the hydrogenation of these nitrobenzene derivatives delivered the desired products with excellent efficiency. Substrates with electron-withdrawing substituents, including halogens, formyl, and carboxyl groups were well tolerated under the reaction conditions, especially at *para* positions. Similarly, nitrobenzene derivatives with electron-donating substituents of methyl, methoxyl, hydroxyl, and amino groups yielded the corresponding amine products selectively and efficiently. Importantly, substituents at *ortho* and *meta* positions did not have a significant impact on the catalytic activity. Overall, these results suggest a broad range of substrates and functional groups were well tolerated by this catalyst.

4. Conclusion

In summary, we report a simple and efficient quenching strategy to create single palladium atoms over cubic indium oxide. The as-generated oxygen vacancies can effectively anchor and confine
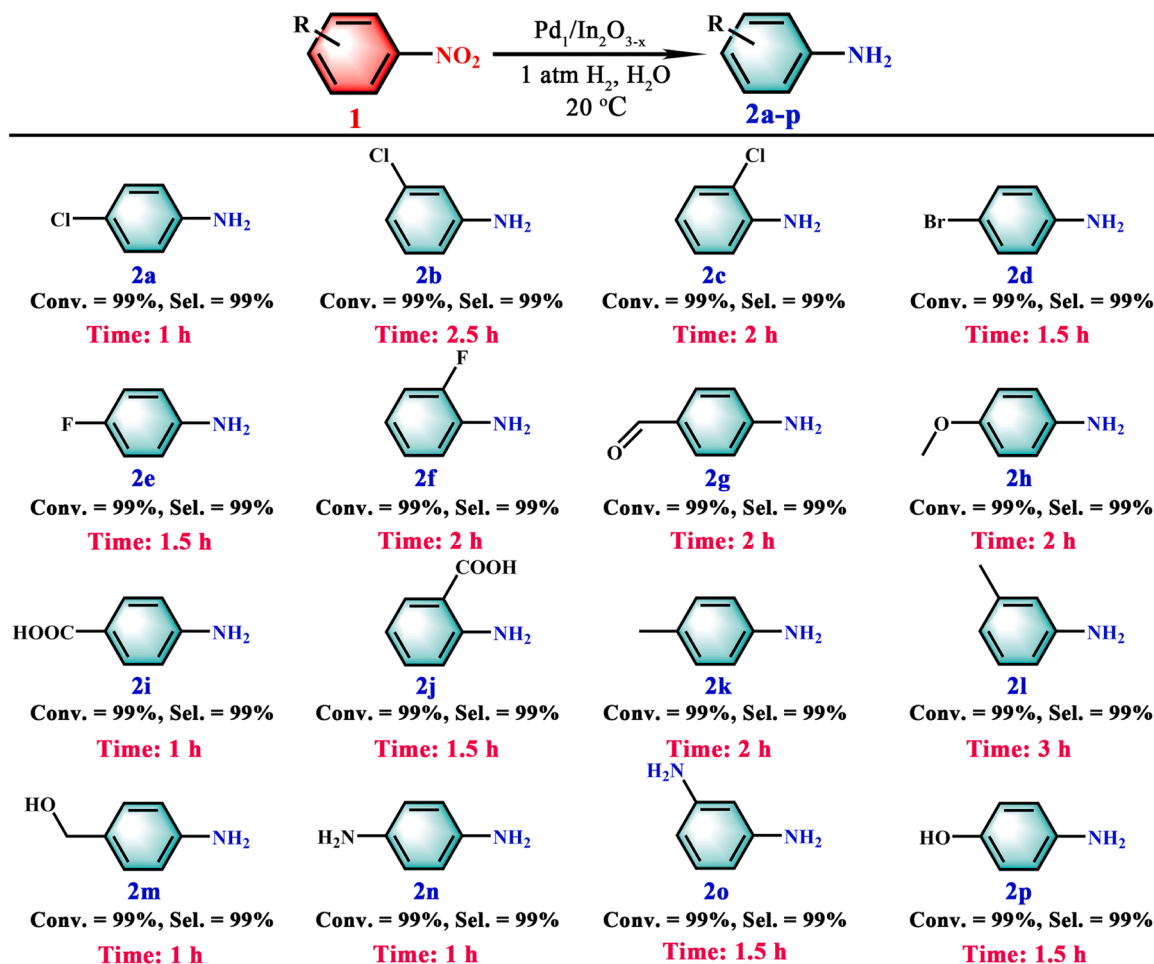
Fig. 5. Hydrogenation of various substituted nitroarenes catalyzed by Pd_1/In_2O_{3-x}.

palladium atoms at the atomic level. The electronic properties of palladium atoms by the metal-support interactions have been elucidated through detailed experimental characterizations and DFT calculations. The Pd_1/In_2O_{3-x} catalyst has shown exceptional efficiency in selectively catalyzing the hydrogenation of nitrobenzene to aniline under green reaction conditions, along with satisfactory recyclability, long-term storage stability, and broad substrate scope. More importantly, it remained high hydrogenation activity even in CO-contaminated hydrogen. DFT calculations further reveal that the Pd1-O4 acted as a highly active site to significantly reduce the energy barriers in the reaction. This quenching strategy provides new insight and may enable controlled synthesis of single atom catalysts by regulating electronic structures of the active sites for industrially important reactions.

CRediT authorship contribution statement

Zhijun Li: Conceptualization, Funding acquisition, Methodology, Project administration, Supervision, Writing – review & editing. **Mingyang Zhang:** Investigation, Methodology, Validation. **Xiuli Dong:** Investigation. **Siqi Ji:** Methodology, Validation. **Lili Zhang:** Investigation. **Leipeng Leng:** Validation, Formal analysis. **Honghong Li:** Formal analysis. **J. Hugh Horton:** Formal analysis. **Qian Xu:** Investigation. **Junfa Zhu:** Validation.

Declaration of Competing Interest

The authors declare that they have no known competing financial interests or personal relationships that could have appeared to influence the work reported in this paper.

Appendix A. Supporting information

Supplementary data associated with this article can be found in the online version at doi:10.1016/j.apcatb.2022.121462.

References

[1] P. Serna, A. Corma, Transforming nano metal nonselective particulates into chemoselective catalysts for hydrogenation of substituted nitrobenzenes, ACS Catal. 5 (2015) 7114–7121.

[2] T.-N. Ye, Y. Lu, J. Li, T. Nakao, H. Yang, T. Tada, M. Kitano, H. Hosono, Copper-based intermetallic electride catalyst for chemoselective hydrogenation reactions, J. Am. Chem. Soc. 139 (2017) 17089–17097.

[3] L. Lin, S. Yao, R. Gao, X. Liang, Q. Yu, Y. Deng, J. Liu, M. Peng, Z. Jiang, S. Li, Y.-W. Li, X.-D. Wen, W. Zhou, D. Ma, A highly CO-tolerant atomically dispersed Pt catalyst for chemoselective hydrogenation, Nat. Nanotechnol. 14 (2019) 354–361.

[4] S. Zhang, C.-R. Chang, Z.-Q. Huang, J. Li, Z. Wu, Y. Ma, Z. Zhang, Y. Wang, Y. Qu, High catalytic activity and chemoselectivity of sub-nanometric Pd clusters on porous nanorods of CeO2 for hydrogenation of nitroarenes, J. Am. Chem. Soc. 138 (2016) 2629–2637.

[5] W.-C. Cheong, W. Yang, J. Zhang, Y. Li, D. Zhao, S. Liu, K. Wu, Q. Liu, C. Zhang, D. Wang, Q. Peng, C. Chen, Y. Li, Isolated iron single-atomic site-catalyzed

chemoselective transfer hydrogenation of nitroarenes to arylamines, ACS Appl. Mater. Interfaces 11 (2019) 33819–33824.

[6] W. Guo, Z. Wang, X. Wang, Y. Wu, General design concept for single-atom catalysts toward heterogeneous catalysis, Adv. Mater. 33 (2021), 2004287.

[7] S. Mitchell, J. Pérez-Ramírez, Single atom catalysis: a decade of stunning progress and the promise for a bright future, Nat. Commun. 11 (2020) 4302.

[8] B. Singh, V. Sharma, R.P. Gaikwad, P. Fornasiero, R. Zbořil, M.B. Gawande, Single-atom catalysts: a sustainable pathway for the advanced catalytic applications, Small 17 (2021), 2006473.

[9] Y. Liu, B. Wang, Q. Fu, W. Liu, Y. Wang, L. Gu, D. Wang, Y. Li, Polyoxometalate-based metal–organic framework as molecular sieve for highly selective semi–hydrogenation of acetylene on isolated single Pd atom sites, Angew. Chem. Int. Ed. 60 (2021) 22522–22528.

[10] Y. Xiong, W. Sun, Y. Han, P. Xin, X. Zheng, W. Yan, J. Dong, J. Zhang, D. Wang, Y. Li, Cobalt single atom site catalysts with ultrahigh metal loading for enhanced aerobic oxidation of ethylbenzene, Nano Res. 14 (2021) 2418–2423.

[11] J. Yang, W.H. Li, S. Tan, K. Xu, Y. Wang, D. Wang, Y. Li, The electronic metal–support interaction directing the design of single atomic site catalysts: achieving high efficiency towards hydrogen evolution, Angew. Chem. Int. Ed. 60 (2021) 19085–19091.

[12] J. Zhang, C. Zheng, M. Zhang, Y. Qiu, Q. Xu, W.-C. Cheong, W. Chen, L. Zheng, L. Gu, Z. Hu, D. Wang, Y. Li, Controlling N-doping type in carbon to boost single-atom site Cu catalyzed transfer hydrogenation of quinoline, Nano Res. 13 (2020) 3082–3087.

[13] Z. Li, X. Lu, W. Sun, L. Leng, M. Zhang, H. Li, L. Bai, D. Yuan, J.H. Horton, Q. Xu, J. Wang, One-step synthesis of single palladium atoms in WO$_{2.72}$ with high efficiency in chemoselective hydrodeoxygenation of vanillin, Appl. Catal. B: Environ. 298 (2021), 120535.

[14] L. Zou, Y.-S. Wei, C.-C. Hou, C. Li, Q. Xu, Single-atom catalysts derived from metal-organic frameworks for electrochemical applications, Small 17 (2021), 2004809.

[15] Z. Li, Y. Chen, X. Lu, H. Li, L. Leng, T. Zhang, Synthesis of cobalt single atom catalyst by a solid-state transformation strategy for direct C-C cross-coupling of primary and secondary alcohols, Nano Res. (2022), https://doi.org/10.1007/s12274-022-4196-7.

[16] Z. Li, L. Leng, X. Lu, M. Zhang, Q. Xu, J.H. Horton, J. Zhu, Single palladium atoms stabilized by β-FeOOH nanorod with superior performance for selective hydrogenation of cinnamaldehyde, Nano Res. 15 (2022) 3114–3121.

[17] Z. Li, H. Li, Z. Yang, X. Lu, S. Ji, M. Zhang, J.H. Horton, H. Ding, Q. Xu, J. Zhu, J. Yu, Facile synthesis of single iron atoms over MoS$_2$ nanosheets via spontaneous reduction for highly efficient selective oxidation of alcohols, Small (2022), 2201092.

[18] Z. Li, D. Wang, Y. Wu, Y. Li, Recent advances in the precise control of isolated single-site catalysts by chemical methods, Natl. Sci. Rev. 5 (2018) 673–689.

[19] D. Liu, A. Barbar, T. Najam, M.S. Javed, J. Shen, P. Tsiakaras, X. Cai, Single noble metal atoms doped 2D materials for catalysis, Appl. Catal. B: Environ. 297 (2021), 120389.

[20] D.T. Tran, D.C. Nguyen, H.T. Le, T. Kshetri, V.H. Hoa, T.L.Luyen Doan, N.H. Kim, J. H. Lee, Recent progress on single atom/sub-nano electrocatalysts for energy applications, Prog. Mater. Sci. 115 (2021), 100711.

[21] H. Xiong, A.K. Datye, Y. Wang, Thermally stable single-atom heterogeneous catalysts, Adv. Mater. 33 (2021), 2004319.

[22] X. Li, A.-E. Surkus, J. Rabeah, M. Anwar, S. Dastigir, H. Junge, A. Brückner, M. Beller, Cobalt single-atom catalysts with high stability for selective dehydrogenation of formic acid, Angew. Chem. Int. Ed. 59 (2020) 15849–15854.

[23] H. Tian, X. Cui, H. Dong, G. Meng, F. Kong, Y. Chen, L. Peng, C. Chen, Z. Chang, J. Shi, Engineering single MnN$_4$ atomic active sites on polydopamine-modified helical carbon tubes towards efficient oxygen reduction, Energy Storage Mater. 37 (2021) 274–282.

[24] Z. Li, H. Li, D. Yuan, L. Leng, M. Zhang, M. Di, J.H. Horton, J. Wang, L. Sun, W. Sun, Photoinduction of palladium single atoms supported on defect-containing γ-AlOOH nanoleaf for efficient trans-stilbene epoxidation, Chem. Eng. J. 429 (2022), 132149.

[25] J. Fonseca, J. Lu, Single-atom catalysts designed and prepared by the atomic layer deposition technique, ACS Catal. 11 (2021) 7018–7059.

[26] J. Kim, S. Choi, J. Cho, S.Y. Kim, H.W. Jang, Toward multicomponent single-atom catalysis for efficient electrochemical energy conversion, ACS Mater. Au 2 (2022) 1–20.

[27] R. Li, L. Luo, X. Ma, W. Wu, M. Wang, J. Zeng, Single atoms supported on metal oxides for energy catalysis, J. Mater. Chem. A 10 (2022) 5717–5742.

[28] B. Liu, Y. Xu, K. Li, H. Wang, L. Gao, Y. Luo, G. Duan, Pd-catalyzed reaction-producing intermediate S on a Pd/In$_2$O$_3$ surface: a key to achieve the enhanced CS$_2$-sensing performances, ACS Appl. Mater. Interfaces 11 (2019) 16838–16846.

[29] J. Wang, C.-Y. Liu, T.P. Senftle, J. Zhu, G. Zhang, X. Guo, C. Song, Variation in the In$_2$O$_3$ crystal phase alters catalytic performance toward the reverse water gas shift reaction, ACS Catal. 10 (2019) 3264–3273.

[30] N. Rui, Z. Wang, K. Sun, J. Ye, Q. Ge, C.-J. Liu, CO$_2$ hydrogenation to methanol over Pd/In$_2$O$_3$: effects of Pd and oxygen vacancy, Appl. Catal. B: Environ. 218 (2017) 488–497.

[31] J.L. Snider, V. Streibel, M.K.A. Hubert, T.S. Choksi, E. Valle, D.C. Upham, J. Schumann, M.S. Duyar, A. Gallo, F. Abild-Pedersen, T.F. Jaramillo, Revealing the synergy between oxide and alloy phases on the performance of bimetallic In–Pd catalysts for CO$_2$ hydrogenation to methanol, ACS Catal. 9 (2019) 3399–3412.

[32] J. Wang, G. Zhang, J. Zhu, X. Zhang, F. Ding, A. Zhang, X. Guo, C. Song, CO$_2$ hydrogenation to methanol over In$_2$O$_3$-based catalysts: from mechanism to catalyst development, ACS Catal. 11 (2021) 1406–1423.

[33] D. Albani, M. Capdevila-Cortada, G. Vilé, S. Mitchell, O. Martin, N. López, J. Pérez-Ramírez, Semihydrogenation of acetylene on indium oxide: proposed single-ensemble catalysis, Angew. Chem. Int. Ed. 56 (2017) 10755–10760.

[34] X. Ye, C. Yang, X. Pan, J. Ma, Y. Zhang, Y. Ren, X. Liu, L. Li, Y. Huang, Highly selective hydrogenation of CO$_2$ to ethanol via designed bifunctional Ir$_1$-In$_2$O$_3$ single-atom catalyst, J. Am. Chem. Soc. 142 (2020) 19001–19005.

[35] M.S. Frei, C. Mondelli, R. García-Muelas, K.S. Kley, B. Puértolas, N. López, O. V. Safonova, J.A. Stewart, D.C. Ferré, J. Pérez-Ramírez, Atomic-scale engineering of indium oxide promotion by palladium for methanol production via CO$_2$ hydrogenation, Nat. Commun. 10 (2019) 3377.

[36] K. Sun, N. Rui, C. Shen, C.-J. Liu, Theoretical study of selective hydrogenation of CO$_2$ to methanol over Pt$_4$/In$_2$O$_3$ model catalyst, J. Phys. Chem. C 125 (2021) 10926–10936.

[37] F. Hu, L. Leng, M. Zhang, W. Chen, Y. Yu, J. Wang, J.H. Horton, Z. Li, Direct synthesis of atomically dispersed palladium atoms supported on graphitic carbon nitride for efficient selective hydrogenation reactions, ACS Appl. Mater. Interfaces 12 (2020) 54146–54154.

[38] Y. Liu, Z. Li, Q. Yu, Y. Chen, Z. Chai, G. Zhao, S. Liu, W.-C. Cheong, Y. Pan, Q. Zhang, L. Gu, L. Zheng, Y. Wang, Y. Lu, D. Wang, C. Chen, Q. Peng, Y. Liu, L. Liu, J. Chen, Y. Li, A general strategy for fabricating isolated single metal atomic site catalysts in Y zeolite, J. Am. Chem. Soc. 141 (2019) 9305–9311.

[39] K. Morgan, A. Goguet, C. Hardacre, Metal redispersion strategies for recycling of supported metal catalysts: a perspective, ACS Catal. 5 (2015) 3430–3445.

[40] G.X. Pei, X.Y. Liu, X. Yang, L. Zhang, A. Wang, L. Li, H. Wang, X. Wang, T. Zhang, Performance of Cu-alloyed Pd single-atom catalyst for semihydrogenation of acetylene under simulated front-end conditions, ACS Catal. 7 (2017) 1491–1500.

[41] L. Wang, Y. Dong, T. Yan, Z. Hu, A.A. Jelle, D.M. Meira, P.N. Duchesne, J.Y.Y. Loh, C. Qiu, E.E. Storey, Y. Xu, W. Sun, M. Ghoussoub, N.P. Kherani, A.S. Helmy, G. A. Ozin, Black indium oxide a photothermal CO$_2$ hydrogenation catalyst, Nat. Commun. 11 (2020) 2432.

[42] F. Gu, M. Di, D. Han, S. Hong, Z. Wang, Atomically dispersed Au on In$_2$O$_3$ nanosheets for highly sensitive and selective detection of formaldehyde, ACS Sens. 5 (2020) 2611–2619.

[43] C. Shen, K. Sun, Z. Zhang, N. Rui, X. Jia, D. Mei, C.-J. Liu, Highly active Ir/In$_2$O$_3$ catalysts for selective hydrogenation of CO$_2$ to methanol: experimental and theoretical Studies, ACS Catal. 11 (2021) 4036–4046.

[44] Z. Cai, J. Dai, W. Li, K.B. Tan, Z. Huang, G. Zhan, J. Huang, Q. Li, Pd supported on MIL-68(In)-derived In$_2$O$_3$ nanotubes as superior catalysts to boost CO$_2$ hydrogenation to methanol, ACS Catal. 10 (2020) 13275–13289.

[45] L. Sun, R. Li, W. Zhan, Y. Yuan, X. Wang, X. Han, Y. Zhao, Double-shelled hollow rods assembled from nitrogen/sulfur-codoped carbon coated indium oxide nanoparticles as excellent photocatalysts, Nat. Commun. 10 (2019) 2270.

[46] Z. Li, W. Wei, H. Li, S. Li, L. Leng, M. Zhang, J.H. Horton, D. Wang, W. Sun, C. Guo, W. Wu, J. Wang, Low-temperature synthesis of single palladium atoms supported on defective hexagonal boron nitride nanosheet for chemoselective hydrogenation of cinnamaldehyde, ACS Nano 15 (2021) 10175–10184.

[47] P. Liu, Y. Zhao, R. Qin, S. Mo, G. Chen, L. Gu, D.M. Chevrier, P. Zhang, Q. Guo, D. Zang, B. Wu, G. Fu, N. Zheng, Photochemical route for synthesizing atomically dispersed palladium catalysts, Science 352 (2016) 797–800.

[48] M.-M. Zhu, X.-L. Du, Y. Zhao, B.-B. Mei, Q. Zhang, F.-F. Sun, Z. Jiang, Y.-M. Liu, H.-Y. He, Y. Cao, Ring-opening transformation of 5-hydroxymethylfurfural using a golden single-atomic-site palladium catalyst, ACS Catal. 9 (2019) 6212–6222.

[49] A. Shanmugasundaram, V. Gundimeda, T. Hou, D.W. Lee, Realizing synergy between In$_2$O$_3$ nanocubes and nitrogen-doped reduced graphene oxide: an excellent nanocomposite for the selective and sensitive detection of CO at ambient temperatures, ACS Appl. Mater. Interfaces 9 (2017) 31728–31740.

[50] Q. Zhang, X.-X. Qin, F.-P. Duan-Mu, H.-M. Ji, Z.-R. Shen, X.-P. Han, W.-B. Hu, Isolated platinum atoms stabilized by amorphous tungstenic acid: metal-support interaction for synergistic oxygen activation, Angew. Chem. Int. Ed. 57 (2018) 9351–9356.

[51] H. Jiang, J. Lin, X. Wu, W. Wang, Y. Chen, M. Zhang, Efficient hydrogenation of CO$_2$ to methanol over Pd/In$_2$O$_3$/SBA-15 catalysts, J. CO$_2$ Util. 36 (2020) 33–39.

[52] Z. Chen, H. Yin, C. Wang, R. Wang, Y. Peng, C. You, J. Li, New insights on competitive adsorption of NO/SO$_2$ on TiO$_2$ anatase for photocatalytic NO oxidation, Environ. Sci. Technol. 55 (2021) 9285–9292.